Icarus 402 (2023) 115602

Contents lists available at ScienceDirect

Icarus

journal homepage: www.elsevier.com/locate/icarus

The brightness of the CO Cameron bands in the martian discrete aurora: A study based on revised cross sections

J.-C. Gérard [a,*], L. Soret [a], B. Hubert [a], L. Neary [b], F. Daerden [b]

[a] LPAP, STAR Institute Université de Liège, Belgium
[b] Royal Institute for Space Aeronomy Brussels, Belgium

ARTICLE INFO

Keywords:
Mars
Aurorae
Spectroscopy
Ultraviolet observations
Atmospheres
Composition

ABSTRACT

We analyze the consequences of the new laboratory measurements of the emissions cross sections of the Cameron bands excited by electron impact on CO_2 and CO in the Mars aurora. We use Monte Carlo simulations to investigate the importance of these changes and their dependence on the initial electron energy. The Mars Climate Database (MCD) is used as an input for the temperature and neutral density profiles. Auroral density profiles of O_2^+, CO_2^+ and electrons in the aurora are calculated for a range of precipitating electron energies. The total nadir brightness of the Cameron bands is reduced by a factor of 4.5 at 150 eV and 5.1 at 700 eV relative to calculations made with the previously recommended cross section. The relative contributions to the production of the Cameron bands by electron collisions with CO_2 and CO are examined. It varies with the CO/CO_2 density ratio near the emission peak that depends on the neutral model and season. Dissociative recombination of CO_2^+ ions provides a contribution between 10% and 45% at the altitude of maximum production of the a $^3\Pi$ state. The efficiency of the nadir brightness of the Cameron bands is 2.5–3.6 kilorayleighs per incident electron energy flux of 1 mW m^{-2}, with a small dependence on the initial electron energy. Model simulations predict that the intensity ratio of the Cameron bands to the CO_2^+ UV doublet (UVD) depends on the electron initial energy. It varies from 2.0 at 500 eV to 5.3 at 50 eV, for both $L_s = 90°$ and 225°.

1. Introduction

The CO a $^3\Pi \rightarrow X\ ^1\Sigma$ Cameron bands between 190 and 270 nm and the CO_2^+ B $^2\Sigma \rightarrow X\ ^2\Pi$ ultraviolet doublet (UVD) at 288–289 nm are among the main spectral features of the Mars and Venus MUV dayglow emissions. Both emissions were initially observed in the dayglow from the Mariner 6 and 7 spacecraft (Barth et al., 1971, 1972; Stewart et al., 1972). Further MUV dayglow observations (Leblanc et al., 2006; Cox et al., 2010; Jain et al., 2015) and models (Fox and Dalgarno, 1979; Jain and Bhardwaj, 2012) confirmed the initial analyses. They concluded that photoionization of CO_2 and electron impact on CO_2 are the dominant dayglow sources of CO_2^+ excited in the $B^2\Sigma_u^+$ state and that photodissociation of CO_2 and dissociative excitation by electron impact are the major sources of the CO($a^3\Pi$) state near the emission peak at ~130 km.

Bertaux et al. (2005) first detected a middle ultraviolet (MUV) auroral emission at the limb with the Spectroscopy for the Investigation of the Characteristics of the Atmosphere of Mars (SPICAM) instrument on board the Mars Express orbiter. The auroral MUV spectrum was very similar to the dayglow spectrum. The aurora was located near the boundary between open and closed crustal magnetic field lines at an estimated altitude of 129 ± 13 km. Leblanc et al. (2008) and Gérard et al. (2015) observed auroral signatures in the nadir direction and analyzed the location and spectral composition of the auroral events. They demonstrated that the bright aurorae tend to concentrate along regions of open crustal magnetic field lines in the southern hemisphere. Soret et al. (2016) determined that the altitude of the maximum Cameron limb brightness was located at 137 ± 27 km. Model simulations indicated that the observed peak altitudes of the auroral MUV emissions correspond to the injection of monoenergetic electrons between 40 and 200 eV. They showed that the peak altitude of the Cameron and UVD bands emissions is identical within the accuracy of the vertical spatial resolution.

A much larger number of discrete auroral events was observed with the Imaging Ultraviolet Spectrograph (IUVS) instrument (McClintock et al., 2015) on board the Mars Atmosphere and Volatile Evolution

* Corresponding author at: Laboratoire de Physique Atmosphérique et Planétaire, Université de Liège, 19c allée du 6 août, Liège B-4000, Belgium.
E-mail address: jc.gerard@uliege.be (J.-C. Gérard).

https://doi.org/10.1016/j.icarus.2023.115602
Received 15 December 2022; Received in revised form 12 April 2023; Accepted 24 April 2023
Available online 9 May 2023

(MAVEN) orbiter. Schneider et al. (2021) detected 278 occurrences of discrete auroral events at the limb. They showed that these events occur primarily in evening hours, especially in a way depending on the orientation of the interplanetary magnetic field. A large number of auroral detections were found to occur far from the crustal magnetic field region. Soret et al. (2021)'s studies of MAVEN-IUVS auroral detections indicated that the histogram of the maximum intensity at the limb ranges between 80 and 160 km, with a maximum probability close to 130 km. Therefore, to convert this altitude of the maximum brightness at the limb to that of the peak of the volume emission rate, two effects must be considered. First, even in the case of a homogeneous emission, the maximum of the peak altitude at the limb is located somewhat lower than the peak of the volume emission rate by the order of one scale height. Second, the confined discrete aurora is not necessarily located at the tangent point of the line of sight. It may originate from a higher altitude in front of or behind the tangent point of any given limb observation (Schneider et al., 2021). Both effects statistically lead to an upward offset of the volume emission rate relative to the maximum of a limb observation. We estimate this offset equal to 10 km and deduce that the maximum emission rate of the Cameron bands is located at ~140 km. Two other types of Mars aurora were later discovered: the extended nightside diffuse aurora (Schneider et al., 2015; Gérard et al., 2017) occurring at lower altitude (~80 km) and the proton aurora (Deighan et al., 2018; Ritter et al., 2018) generally observed on the dayside.

Simultaneous detections of FUV auroral signatures by SPICAM and in situ measurements of electron precipitation with the ASPERA 3-ELS electron analyzer showed a close correlation between both types of events. The nadir brightness of the Cameron bands ranged from 0.12 to 1.9 kiloRayleigh (kR, 1 kR = 10^9 photons cm^{-2} s^{-1} per 4π steradians) per incident electron energy flux of 1 mW m^{-2}. Soret et al. (2021) analyzed the relation between five discrete auroral events detected at the limb by IUVS and the integrated incoming electron energy flux measured by the Solar Wind Electron Analyzer (SWEA) detectors between 50 and 2000 eV on board MAVEN. One event is of particular interest as the optical and electron precipitation detection occur simultaneously at a time when the location of the MAVEN spacecraft and the tangent point of the line of the IUVS sight were only separated by 260 km. This coincidence occurred during MAVEN orbit 3520 at 11:02:12 UT and was illustrated in their Fig. 9a. The limb brightness of the Cameron bands was 1.8 kR and the electron flux measured by SWEA reached 1.1 mW m^{-2}. A second case of simultaneous electron enhancement of 2.7 mW m^{-2} and an auroral emission of 4.1 kR were detected during orbit 8627. These measurements correspond to efficiencies of 1.6 and 1.5 kR/mW m^{-2}. These efficiencies are near the upper range of the combined ASPERA-SPICAM detections.

The Cameron/UVD intensity ratio was examined in three different studies. Gérard et al. (2015) re-analyzed the full nadir viewing SPICAM database and identified 16 auroral events in the southern hemisphere. The mean Cameron/UVD intensity ratio was 4.9 in the nadir direction as measured through the wide SPICAM slit. The three limb viewing detections by Soret et al. (2016) with SPICAM provided a mean intensity ratio of 9. Soret et al. (2021) found that the Cameron and UVD brightness at the limb observed with IUVS-MAVEN generally co-varies with a mean ratio of 6.6, although the low intensity cases tend to show a lower ratio while larger values are observed in bright aurorae. They also confirmed that the altitudes of both emissions are very close to each other over a range of peak altitudes extending between 80 and 160 km.

Models of the Martian auroral MUV emissions have been described by Soret et al. (2016), Bisikalo et al. (2017), Gérard et al. (2017) and Soret et al. (2021). They all used a Monte Carlo electron transport model (Gérard et al., 2008) adapted to the Mars atmosphere to study the vertical and limb intensity of auroral emissions caused by precipitation of energetic electrons. The neutral density altitude distribution was taken from the M-GITM model (Bougher et al., 2015) adapted to conditions of the IUVS detection of the aurora. The model calculated the dependence of the altitude variation of the auroral emissions versus the electron initial energy. It was used to investigate the production of the CO Cameron and Fourth Positive bands, the CO_2^+ UV doublet, the 130.4 nm and 297.2 nm oxygen emissions. The present study updates earlier analyses of the CO Cameron and CO_2^+ UVD emissions at Mars using newly determined cross sections.

In section 2, we describe the sources of the excited a $^3\Pi$ state and the previously used emission cross sections. Section 3 describes the new excitation cross sections and the differences with those previously used in the literature. New Monte Carlo simulations of the auroral sources of the Cameron bands and comparisons with earlier results are presented in section 4. Section 5 discusses the uncertainties in the CO abundance and section 6 the dependence of spectral distribution of the Cameron bands versus the electron energy.

2. Auroral sources of Cameron bands

The main sources of a $^3\Pi$ state in the aurora are:

$$CO_2(X^1\Sigma) + e_f\ (E > 11.5\ eV) \rightarrow CO(a^3\Pi) + O + e'_f \quad (1)$$

$$CO(X^1\Sigma^+) + e_f\ (E > 6\ eV) \rightarrow CO(a^3\Pi) + e'_f \quad (2)$$

$$CO_2{}^+(X^2\Pi_g) + e_{th} \rightarrow CO(a^3\Pi) + O \quad (3)$$

The CO_2^+ UV doublet is produced by electron impact on CO_2:

$$CO_2(X^1\Sigma) + e_f\ (E > 18.1\ eV) \rightarrow CO_2{}^+(B^2\Sigma) + e' + e'' \quad (4)$$

where e_f and e_{th} denote fast auroral and thermal electrons respectively.

Previous model calculations lead to the conclusions that electron impact on CO_2 (process 1) is the dominant production of CO a $^3\Pi$ state in the lower thermosphere while processes (2) and (3) are secondary sources. The electron impact cross sections for (1) and (2) were based on the initial laboratory measurement by Ajello (1971a, 1971b). The recommended value of the peak of the e + CO_2 cross section was 2.410^{-16} cm^2 near 100 eV (Avakyan et al., 1999; Shirai et al., 2001; Bhardwaj and Jain, 2009), based on the early measurements by Ajello (1971a) and renormalized at 80 eV by Erdman and Zipf (1983) who corrected for the lifetime and presence of other transitions. To account for re-measurements of the radiative lifetime of the a $^3\Pi$ metastable state and obtain agreement with the Cameron dayglow observations, several dayglow modelers reduced the magnitude of the cross section by a constant factor of 2 to 3 at all energies (Conway, 1981; Gronoff et al., 2012; Jain and Bhardwaj, 2012; González-Galindo et al., 2018). Fox and Dalgarno (1979, 1981) used lower peak values such as 4×10^{-17} cm^2 at 27 eV, based on the measurements by Freund (1971). These corrections reduced the brightness of the simulated Cameron bands dayglow model, although the presence of other source processes limited the impact of this downward revision. Soret et al. (2016, 2021) also adopted a value of 8×10^{-17} cm^2 at 80 eV in their auroral model calculations. Similarly, Gérard et al. (2017) applied a downward scaling factor of 3 in their model of the Martian diffuse aurora. The contribution of process (1) decreases linearly with the scaling factor. The value of the cross section for electron impact on CO by Shirai et al. (2001) was also based on laboratory measurements by Ajello (1971b) and renormalized at 11 eV by Erdman and Zipf (1983). It reaches a peak of 1.4×10^{-16} cm^2 at 11 eV, close to the excitation threshold.

In the next sections, we analyze the consequence of the new measurements on the model and discuss the relative importance of processes (1) and (2).

3. New emission cross sections

Recent laboratory measurements shed a new light on the difficulty of laboratory measurements of the Cameron bands emission cross sections.

In brief, Lee et al. (2021, 2022) have found that the initial cross section measurements were flawed as a consequence of the wall effects on the measurements of relatively long radiative lifetime of the metastable a $^3\Pi$ state in an insufficiently large vacuum chamber. The high-velocity CO (a $^3\Pi$) fragments were deactivated in collisions with the chamber walls. In addition, the Cameron bands were not completely spectrally resolved at the instrument's resolution and partly blended with the CO Fourth Positive bands. Lee et al. (2022) recommended to discard the previous work by Ajello (1971b) and use their new values, based on more accurate work carried out in a much larger tank at the University of Colorado. Their experiments avoid the effects of spectral blending, includes the entire band system between 180 and 280 nm, and carefully accounts for the kinetic energy imparted drift out of the detector field of view from dissociative excitation of CO_2.

Similarly, a revised cross section for process (2), although less dramatic, was also measured by Lee et al. (2021).

A comparison between the earlier cross sections and the analytical fit to those measured by Lee et al. (2021, 2022) is shown in Fig. 1. The dotted lines correspond to the values from Shirai et al. (2001) in red for e + CO_2 and in blue for e + CO. The solid lines represent the analytical fits to the new measurements by Lee et al. (2021, 2022). We note that the new laboratory measurements were made at a limited number of electron energies. The electron impact cross section on CO_2 is strongly different from the earlier one. The peak value is less by a factor of 6 and the shape is drastically different. The Lee et al. (2022) cross section rapidly drops beyond 20 eV, in contrast with the Avakyan-Shirai cross section which remains quite flat between 20 and 300 eV. At 100 eV, the two values differ by more than two orders of magnitude. For e + CO, the peak value is close to the earlier value recommended by Shirai et al. (2001) but the new cross section decreases much more rapidly with increasing electron energy beyond 15 eV. Below 15 eV, we adopt the cross section recommended in Table 1 by Furlong and Newell (1996) normalized to the value measured at 15 eV by Lee et al. (2021).

We now examine the consequences of the adoption of the Lee et al. (2021, 2022) new values on the Monte Carlo simulations of the intensity of the Cameron bands and the Cameron/CO_2^+ UVD ratio in the aurora. In particular we discuss the relative importance of sources (1) and (2).

4. Monte Carlo model simulations

In this section, we first briefly describe the Monte Carlo model used to simulate the emission rate of the Cameron and UV doublet bands. We then describe the results of the model calculations for different initial electrons and seasons including the altitude of the peak emission and the Cameron/UVD intensity ratio.

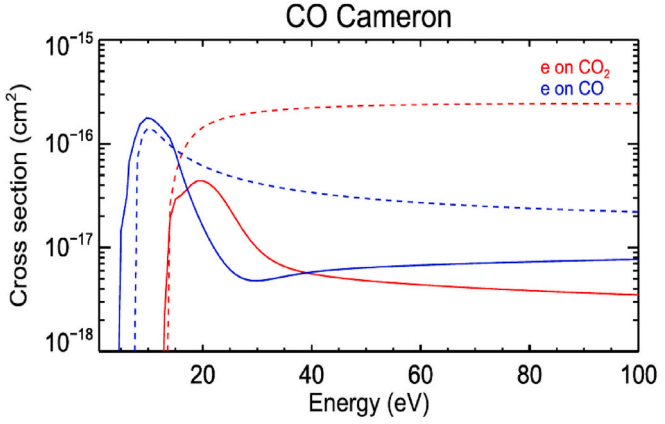

Fig. 1. Comparison of the excitation cross section of the CO Cameron bands by electron impact on CO_2 (red) and CO (blue). The dotted lines show the analytical expressions by Shirai et al. (2001) and the solid lines correspond to the fits to new measurements by Lee et al. (2021, 2022). (For interpretation of the references to colour in this figure legend, the reader is referred to the web version of this article.)

4.1. The model

The electron transport and excitation model used for the following numerical simulations was initially developed by Shematovich et al. (2008) for the Martian dayglow, Gérard et al. (2008) for the Venus aurora and dayglow and Soret et al. (2016) for the Mars aurora. The method was originally derived from a kinetic model for the hot oxygen geocorona by Shematovich et al. (1994). It is based on photochemical processes, kinetics and a Monte Carlo approach. Auroral electrons interact with the Martian atmosphere where they lose their kinetic energy in elastic, inelastic and ionizing collisions with the ambient atmospheric gas. The energy loss of the precipitating electrons is calculated by solving the kinetic equation, involving the transport of electrons, the production of primary and secondary electrons and elastic and inelastic scattering terms. The Monte Carlo algorithm numerically solves the Bolzmann's kinetic equations for atmospheric systems using the Direct Simulation Monte Carlo approach. The model outputs are the vertical distributions of volume emission rates of various CO, CO_2^+ and O emissions between 30 km and 300 km. The atmospheric model in the following simulations is provided by the Mars Climate database (MCD) (version 5.3) (Forget et al., 1999; González-Galindo et al., 2009; Millour et al., 2019) for conditions appropriate to the largest number of detections of the nightside discrete aurora: latitude = 50°S, planetary longitude $L_s = 180°$, local time = 00:00 h, solar longitude = 90°. We use the winter solstice season in the southern hemisphere as our base case since this is the most favorable period for nightside observations in the crustal field region. The temperature and neutral atmosphere composition are shown in Fig. 2.

The emission cross sections of the main auroral spectral features were listed by Gérard et al. (2017). They have been used for this study with a few exceptions. In particular, the cross sections for processes (1) and (2) initially taken from Shirai et al. (2001) have been replaced by the new values from Lee et al. (2021, 2022). The emission cross section for the CO_2^+ UV doublet is taken from the recommended values by Itikawa (2002), based on Tsurubuchi and Iwai (1974) measurements.

The contribution of process (3) is given by the product $\alpha CO_2^+ \times \varepsilon \times [CO_2^+] \times Ne$, where $[CO_2^+]$ is the CO_2^+ ion density and Ne the electron density. The dissociative recombination coefficient of CO_2^+, $\alpha CO_2^+ = 4.2 \times 10^{-7}\ (300/T_e)^{0.75}$ is taken from Viggiano et al. (2005), confirmed by Fournier et al. (2013). The efficiency ε of the production of the a $^3\Pi$ state is equal to 0.29 ± 0.10 (Skrzypkowski et al., 1998; Rosati et al., 2003). The steady state calculation of the CO_2^+ and electron densities follows a simplified version of the ionospheric scheme by González-Galindo et al.

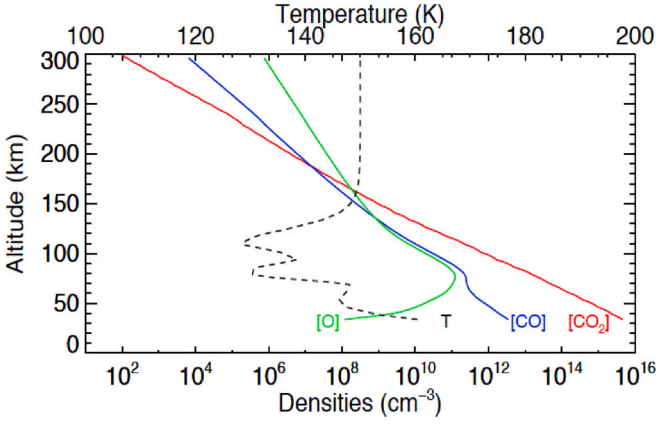

Fig. 2. MCD model atmosphere used for the numerical simulations of auroral brightness distribution in this study ($L_s = 90°$).

(2013). In the lower thermosphere, the CO_2^+ ions created by the collisions of the electrons with CO_2 readily transfer their charge to atomic oxygen to form O_2^+. In the lower thermosphere, a photochemical balance is established between the CO_2^+ and the O_2^+ ions. The energy dependent cross section for the production of CO_2^+ ions by electron impact is taken from Itikawa (2002). This calculation is valid in the region below about 200 km where photochemical control is dominant (Fox et al., 2017), which corresponds to the altitude range where the bulk of the Cameron bands is emitted. At higher altitude, plasma transport processes become important and have been ignored here. Under these conditions, the CO_2^+ density is given by:

$$[CO_2^+] = \frac{P(CO_2^+)}{(k_1 + k_2)[O] + \alpha_{CO_2^+} N_e}$$

where $P(CO_2^+)$ is the production rate of CO_2^+ ions, $k_1 = 9.6 \times 10^{-11}$ cm^3 s^{-1} and $k_2 = 1.6 \times 10^{-10}$ cm^3 s^{-1} are the rate coefficients of the $CO_2^+ + O \rightarrow CO_2 + O^+$ and $CO_2^+ + O \rightarrow CO + O_2^+$ reactions respectively. The electron temperature in the aurora is taken equal to the neutral temperature since our model does not include the calculation of the energy balance in the ionosphere for a given auroral energy flux and mean energy. This simplification leads to an overestimate of the $CO_2^+ + e$ source of CO a $^3\Pi$ molecules. For example if $T_e = 500$ K, the maximum volume production rate of Cameron bands by CO_2^+ recombination would decrease by about 30%.

Fig. 3 shows the density profiles of both ions calculated for two different initial electron energies. The determination of the O_2^+ density, the dominant ion in the region of interest here, is important to calculate the electron density N_e that controls the CO_2^+ ion density in the above expression. The calculated $[O_2^+]/[CO_2^+]$ ratio at the peak increases from 5.3 for a 50 eV precipitation to 13 at 1 keV. These densities and their ratio are comparable to those measured in the dayside ionosphere (Haider et al., 2011; Yoshida et al., 2021). This similarity is expected as the ratio between the two species is independent of the initial mechanism creating the CO_2^+ ions.

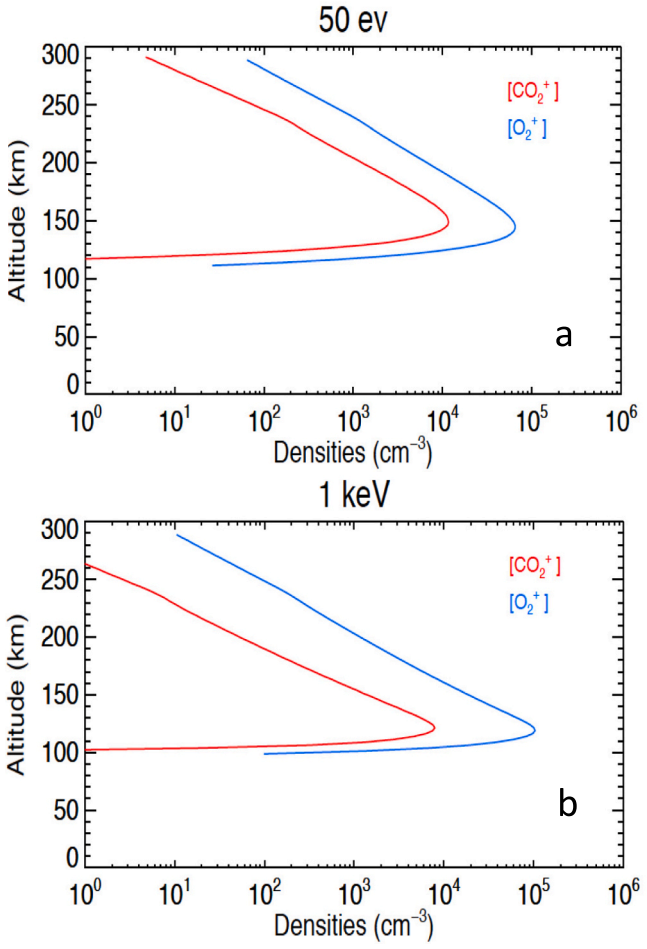

Fig. 3. Calculated vertical distribution of the O_2^+ and CO_2^+ density for initial electron energies of 50 eV (a) and 1 keV (b). The integrated electron energy flux is 1 mW m^{-2} in both cases and the solar longitude $L_s = 90°$.

4.2. CO abundance in the nightside lower thermosphere

The abundance of CO in the lower thermosphere is only loosely constrained by in situ or remote sensing observations. The Viking mass spectrometers (Nier and McElroy, 1977) give a CO/CO_2 density ratio of about 0.05 at 140 km. More recently, the NGIMS mass spectrometer on board MAVEN measured molecular mass 28 down to 120 km during deep dip sequences. Mahaffy et al. (2015) reported a CO/CO_2 ratio of about 0.01 at 135 km. However, there is an ambiguity with N_2 which has an identical molecular mass and the accuracy of the density of the CO density is limited. It has subsequently been challenged (Wu et al., 2020), so that the CO/CO_2 density ratio in the lower thermosphere thus remains somewhat uncertain. Occultation measurements of this ratio on board the Trace Gas Orbiter are limited to altitudes below 100 km (Yoshida et al., 2022). However, the column density ratio between CO and CO_2 was recently derived by Evans et al. (2022) from measurements of the CO Fourth Positive bands with the Emirates Ultraviolet Spectrometer (EMUS) on board the HOPE Emirates Mars Mission. They found that the column abundance of CO relative to CO_2 above ~70 km is systematically larger than the MCD simulations by ~40%. The variability in local time, latitude and solar longitude of the CO relative column abundance observed by EMUS was generally different from the MCD predictions. For consistency, in this study we have adopted the CO density distribution provided by the MCD as was shown in Fig. 2. Fig. 4 illustrates the vertical distribution of the CO/CO_2 density ratio from the MCD under the conditions used in this study. In the base case ($L_s = 90°$, solid line), the ratio is about 0.1 at 140 km and reaches unity close to 200 km.

This ratio varies not only with altitude but also with season and latitude. For comparison, this ratio is also shown at the same location for $L_s = 225°$ when it is significantly smaller. The Mars Climate Model predicts that the CO/CO_2 ratio varies at 130 km from 0.02 at $L_s = 270°$ to 0.21 at $L_s = 75°$ at 50° S, 00:00 local time. This latitudinal-seasonal change, if real, will significantly modulate the relative importance of the a $^3\Pi$ state production by electron impact on CO_2 and CO as a function of L_s. In contrast, the GEM-Mars model (Neary and Daerden, 2018;

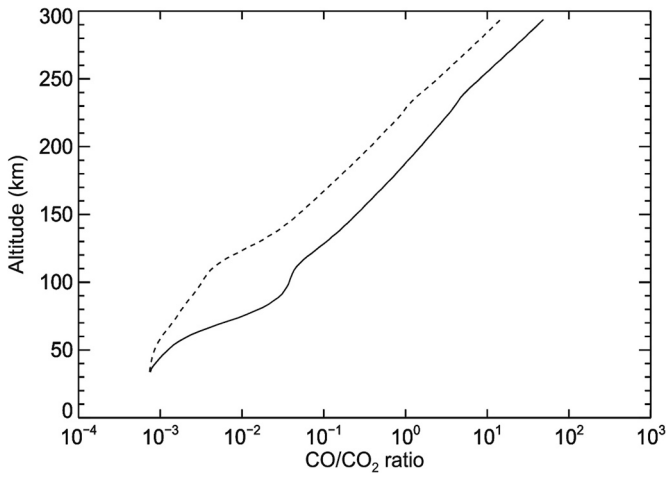

Fig. 4. Altitude variation of the CO/CO_2 density ratio in the MCD used in this study. The solid line corresponds to $Ls = 90°$ and the dashed line to $L_s = 225°$.

Daerden et al., 2019) gives density ratios between 0.01 ($L_s = 120°$) and 0.02 ($L_s = 200°$), globally smaller and more constant throughout the Martian year than the MCD (see supplemental material for a comparison of the seasonal variation in the two models).

4.3. Results

The relative importance of processes (1), (2) and (3) in the production of the a $^3\Pi$ state is illustrated in Fig. 5 for two different seasons and three initial electron energies, all for a precipitated electron energy flux of 1 mW m^{-2}. Cases (a) and (c) correspond to $L_s = 90°$ and (b) and (d) to $L_s = 225°$ to cover periods of maximum and minimum CO/CO_2 ratio predicted by the MCD (see Supplemental Material). Energies in panels (c) and (d) correspond to a maximum production near 140 km. At $L_s = 90°$ processes (1) and (2) equally contribute to the total emissions rate near the peak, reaching a maximum of 1.1×10^3 cm^{-3} s^{-1} at 141 km for E = 50 eV (case a) and 1.2×10^3 at 139 km for E = 100 eV (case c). At higher altitude, impact on CO progressively dominates the production of the Cameron bands as the CO/CO_2 density ratio increases. The contribution of process (2) is directly proportional to the CO density. It makes a smaller but significant contribution with a maximum contribution about ~10 km higher than the electron impact sources. The relative importance of the three sources remains nearly unchanged near the peak between (a) and (c). Similar curves for $L_s = 225°$, E = 50 eV and E = 500 eV are shown in panels (b) and (d). Comparison between (b) and (a) indicates that the production peak has moved up by 12.5 km, a consequence of the thermal expansion and upward displacement of the isobar levels when Mars moves closer to perihelion. The maximum volume emission rate is 1.4×10^3 cm^{-3} s^{-1}. In this case again, recombination of CO_2^+ ions is a third but important contribution. Cases (a) and (d) produce peak productions at the same altitude near 140 km, in agreement with the MAVEN-IUVS limb observations showing a statistical apparent maximum of the peak altitude near 130 km (Soret et al., 2016, 2021). In both cases, the importance of the electron impact on CO is reduced relative to $L_s = 90°$ as a consequence of the smaller CO/CO_2 density ratio predicted by the MCD model during winter summer.

Comparative simulations for the identical conditions show that the calculated nadir brightness of the Cameron bands has decreased by a factor of 4.5 at 150 eV and 5.1 at 700 eV relative to calculations with the Avakyan-Shirai cross section. The difference essentially stems from the reduction and modified shape of the e + CO_2 cross section.

Fig. 6a shows the calculated total volume emission rate of the Cameron bands and CO_2^+ UV doublet resulting from electron impact on CO_2 and CO as well as CO_2^+ dissociative recombination for a series of initial electron energies ranging from 30 to 1000 eV. The total energy flux on the top of the model is 1 mW m^{-2} in all simulated cases. As expected, the altitude of the peak of the Cameron bands decreases with increasing initial electron energy, but the maximum production rate remain nearly constant at a value between 1.0×10^3 and 1.4×10^3 cm^{-3} s^{-1}.

The variation of the peak altitude is best seen in Fig. 7 where the maximum of the Cameron bands production is represented versus the electron energy. It shows that the altitude of maximum production remains quasi constant at 139 km for energies up to ~150 eV at $L_s = 90°$. Beyond this energy, it monotonically drops down to 119 km at 1 keV. These altitudes are somewhat higher than those calculated by Soret et al. (2016) owing to the different model atmosphere and the increased importance of electron impact on carbon monoxide. The corresponding vertical brightness is between 2.5 and 3.6 kR per incident electron flux of 1 mW m^{-2}. These values may be compared to Xu et al. (2022a) who empirically determined an efficiency of ~4 kR/mW m^{-2} for observations at the limb.

We now examine the behavior of the CO_2^+ UV doublet emission for the same conditions as the Cameron bands. Fig. 6b illustrates the increase in magnitude and the decrease in altitude of the maximum emission rate as the electron energy increases. Its magnitude changes by a factor of 10 from 30 eV to 1 keV and the altitude drops from 152 to 120 km. The vertically integrated brightness increases from 3.3 kR at 30 eV and stabilizes at 21 kR beyond 100 eV. The different energy dependence of the two emissions is partly a consequence of the different excitation thresholds (18.1 eV for UVD versus 6.0 and 11.5 eV for the Cameron bands) and the erosion of the higher-energy electron as the beam penetrates into the atmosphere as shown is section 5. In the case of electrons with energy less than a few hundred eV, the contribution of processes (2) and (3) show a maximum at a higher altitude than process (1) as illustrated in Fig. 5. Therefore, the peak of the total production rate of the

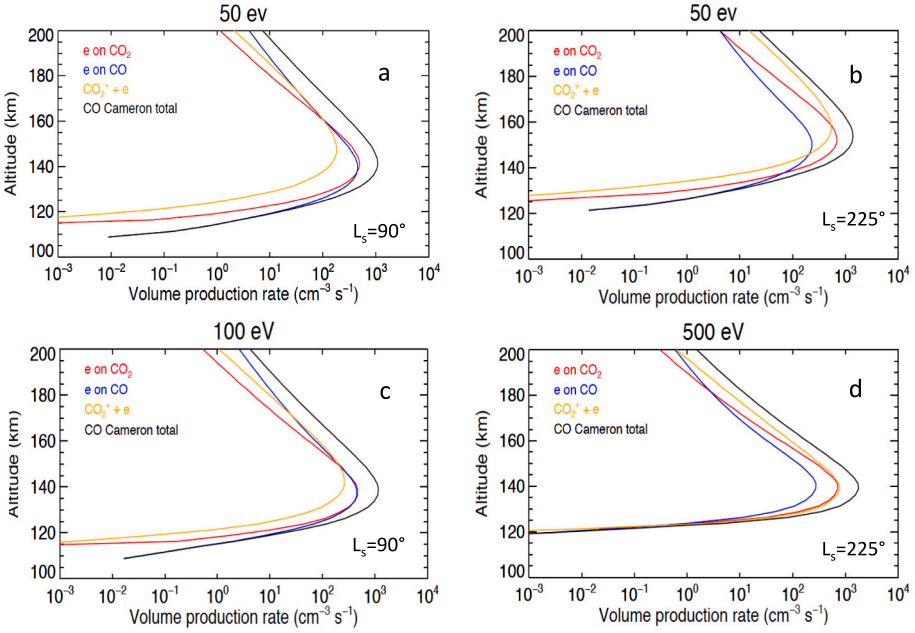

Fig. 5. Calculated contributions of electron impact on CO_2 and CO to the volume production rate of a $^3\Pi$ state at two seasons (left column: $L_s = 90°$; right column: $L_s = 225°$) and different electron energies carrying an energy flux of 1 mW m^{-2}.

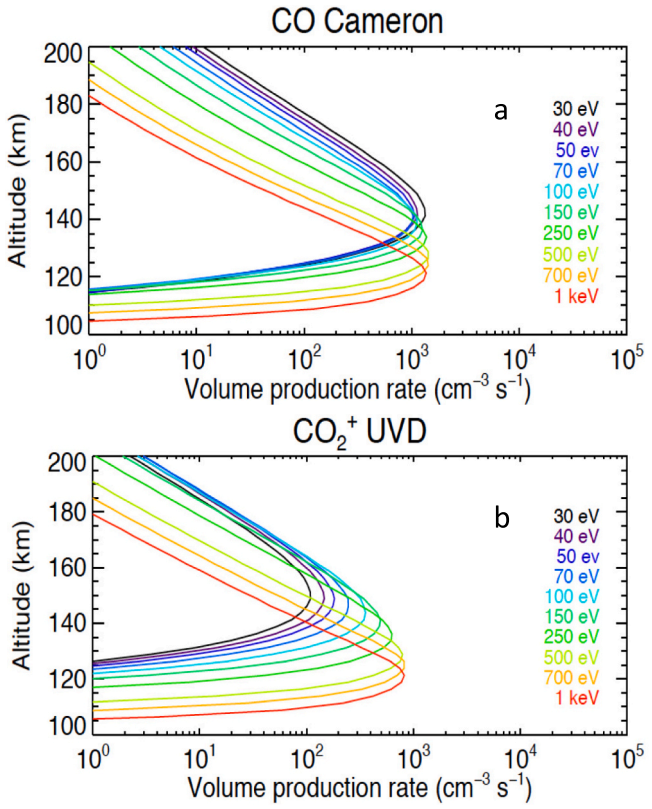

Fig. 6. (a) Volume production rate of the a $^3\Pi$ state leading to the production of the Cameron bands for different initial electron energies; (b) Volume production rate of the B $^2\Sigma$ state producing the CO_2^+ ultraviolet doublet. The curves show the sum of the contributions from electron impact on CO_2 and CO and CO_2^+ dissociative recombination for the Cameron bands and from impact on CO_2 for the UV doublet. The electron energy flux is 1 mW m^{-2} in both cases and the solar longitude $L_s = 90°$.

Cameron bands shows an offset from that of the UVD when the electron energy decreases. This is best seen in Fig. 7 showing the progressive separation of the two peak altitudes for decreasing energies less than 500 eV for both $L_s = 90°$ and 225°. Below ~50 eV, this offset remains close to 20 km.

The calculated nadir intensity of the two emissions shows a different energy dependence as illustrated in Fig. 8. In agreement with the results of Fig. 6, the Cameron band peak value and nadir intensity shows little variation as the energy varies from 30 eV to 1 keV. Fig. 8a presents the nadir intensity remaining close to 3 kR for a precipitated flux of 1 mW m^{-2} (black lines) at both L_s values (dashed and solid lines). This quasi-constant value is in contrast with the UVD brightness that increases with increasing electron energy between 30 and 500 eV (blue lines). Fig. 8b shows the corresponding energy dependence of the Cameron/UVD intensity ratio. Our simulations predict a drop of the intensity ratio from 11.5 at 30 eV to 1.7 at 1 keV common to both solar longitudes. As mentioned before, the mean ratio observed in the discrete aurora is about 4.9 at the nadir from Mars Express-SPICAM and 6.6 at the limb from MAVEN-IUVS. These two ratios correspond to 40 and 55 eV respectively for $L_s = 90°$ (solid line). We note that these two curves depend on the neutral model adopted that varies with latitude and season. In particular, the relative importance of process (2) is directly dependent on the CO/CO_2 density ratio as discussed in section 4.2. This ratio varies not only with altitude but also with season and latitude.

5. Spectral distribution

The measured spectral distribution of the Cameron bands between 170 and 270 nm and its dependence on the electron energy have been discussed by Lee et al. (2021, 2022). They showed that the impact of electrons with energies less than 20 or 30 eV on CO_2 produces a spectral distribution matching well the IUVS dayglow and auroral spectra described by Soret et al. (2021). In contrast, laboratory spectra at 100 eV show a totally different spectral distribution with a single strong peak near 193 nm that is absent in the Martian observations. Collisions of 15 eV electrons with CO produce the same Cameron band distribution as observed in the aurora, but the relative intensity of the (2,0), (1,0) (0,0) and (0,1) bands is somewhat different from the Martian spectra. In particular, the intensity of the (1,0) band appears too strong relative to

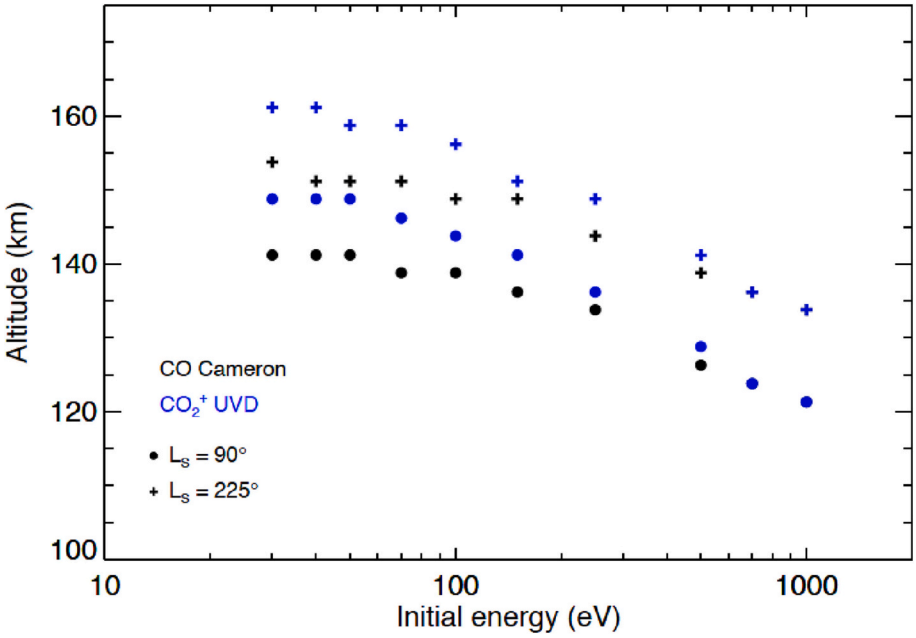

Fig. 7. Variation of the altitude of the emission peak of the Cameron bands (black symbols) and CO_2^+ UVD (blue symbols) with the initial electron energy. Dots and crosses refer to $L_s = 90°$ and 225° respectively. Above 600 eV, the black and blue symbols coincide.

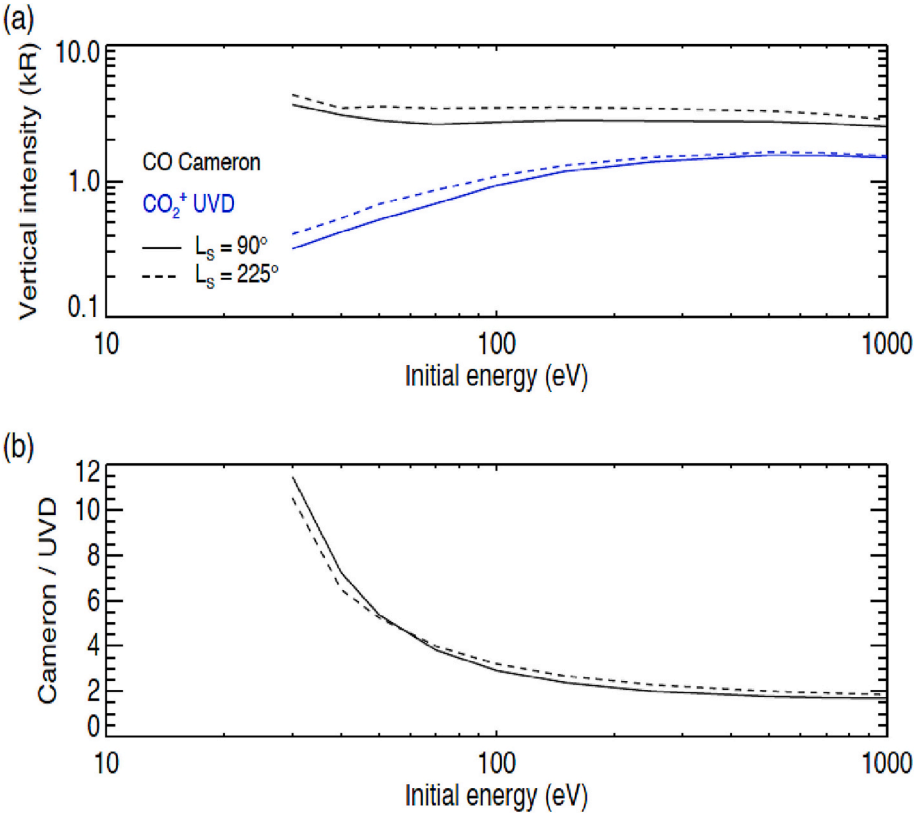

Fig. 8. (a) Vertically integrated brightness of the Cameron and UV doublet as a function of the initial electron energy electron; (b) Intensity ratio of the two emissions. Solid lines correspond to $L_S = 90°$ simulations and dashed lines refer to $L_S = 225°$.

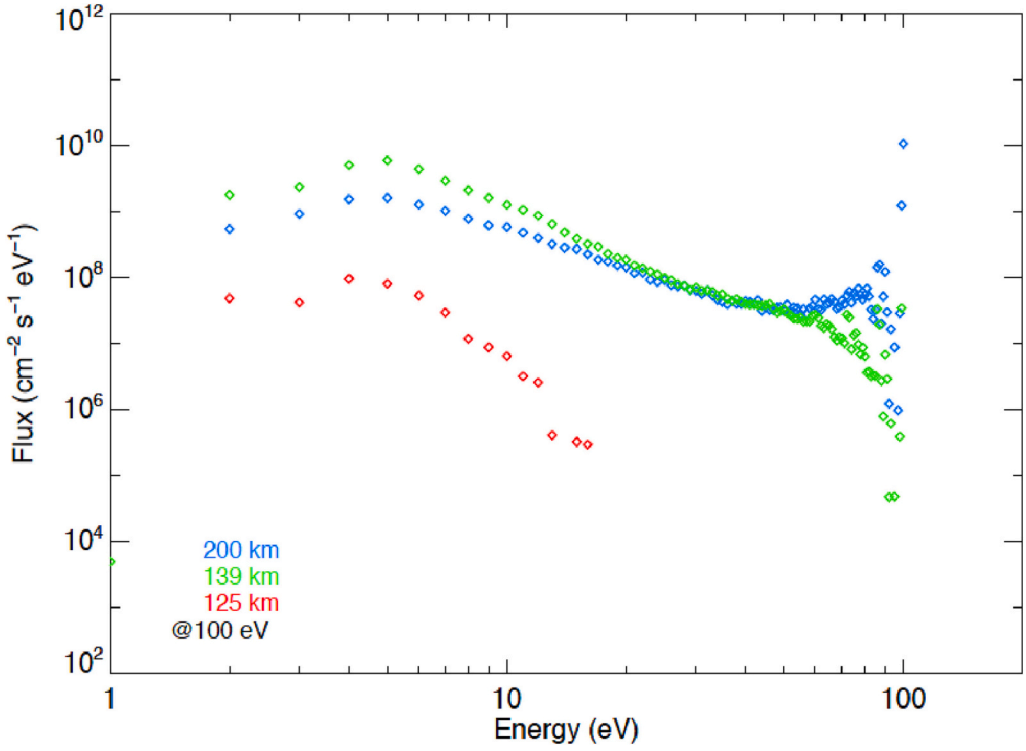

Fig. 9. Electron energy spectra of the flux at 200 km (blue), 139 km (green) and 125 km (red) calculated with the Monte-Carlo electron transport model for a beam of 100 eV initial energy. (For interpretation of the references to colour in this figure legend, the reader is referred to the web version of this article.)

the other bands. Excitation by 30 and 100 eV electrons produce radically different spectral distributions: the CO Fourth Positive and CO^+ First Negative bands become dominant respectively, unlike in the observations. Finally, we note that the intensity distribution of the Cameron bands in the laboratory spectrum resulting from the CO_2^+ dissociative recombination by Skrzypkowski et al. (1998) is very similar to the auroral and dayglow spectra observed with SPICAM and IUVS.

The bulk of the electrons producing the Cameron bands near the peak altitude have also suffered collisions with the neutral gas. It is a mixed population of energy-degraded primary electrons and secondary electrons.

The global energy distribution of this mixed population is calculated at each altitude by the Monte Carlo model. As an example, Fig. 9 presents the calculated electron flux at three different altitudes for $L_s = 90°$. As expected, the initially monoenergetic energy (100 eV) beam is progressively eroded by elastic and inelastic collisions with neutrals which contributes to populate the lower energy electrons and remove the higher energy component. Near the peak altitude (139 km, green diamonds), it has almost completely disappeared. At this altitude, the mean electron energy is 9.2 eV. At lower altitude, under the emission peak, the flux has drastically decreased and only electrons below ~15 eV are still present at 125 km (red diamonds). The mean electron energy increases to 11.4 eV at 134 km for electrons with an initial energy of 250 eV.

In summary, impact on CO_2 of electrons with energy less than a few tens of eV and dissociative recombination of CO_2^+ ions produce Cameron bands with a spectral distribution similar to that observed in the aurora. Electron impact on CO generates a spectrum compatible with the auroral observations if their energy is above 6 eV but less than 30 eV. This energy range is thus compatible with our estimate of the mean energy of the electrons in the region of the emission peak.

6. Discussion and conclusions

Recent measurements of the emission cross sections of the CO Cameron bands by electrons show significant differences with earlier values frequently used to model the Martian aurora and airglow distribution. They modify the relative importance of the electron impact on CO_2 and CO, the relation between the incident auroral electron flux, the Cameron band intensity and the energy dependence of the Cameron/CO_2^+ intensity ratio. Owing to the decrease of the collisional excitation sources, dissociative recombination of CO_2^+ ions becomes a more important source of $a^3\Pi$ CO molecules, with an importance depending on the neutral atmosphere and the electron energy. This contribution varies from 10% to 45% of the total production at the altitude of the production peak in the cases considered here.

Only a few concurrent measurements of nadir brightness and precipitating electron flux have been reported in the literature. The geographical coincidence of the two measurements is critical. Nadir observations have indicated that the spatial extension of the aurora is frequently limited to a few tens of kilometers along the latitudinal direction (Gérard et al., 2015; Lillis et al., 2022). Xu et al. (2022a) analyzed the quantitative relation between the discrete auroral emission detected at the limb by MAVEN-IUVS and the integrated electron energy flux measured by the SWEA detectors between 50 and 2000 eV. The auroral electron fluxes were measured at night in the one-sided loss cone between 170 and 500 km. They found that the empirical linear relation between the logarithm of the two quantities could be statistically summarized by the expression $\log(\phi_e) = 0.23 \log(\mathrm{I(Cameron)})$, where ϕ_e is the incident energy flux in mW m^{-2} and I(Cameron) the limb intensity measured with IUVS during the corresponding auroral event (Xu et al., 2022a, supplementary information). The corresponding efficiency of the Cameron band production is 4 kR of Cameron limb brightness at the limb per incident mW m^{-2}, a value close to the predicted nadir intensities shown in Fig. 8a. The auroral events used for the MAVEN-IUVS extensive brightness-electron flux comparisons were made at the limb. In this geometry, the horizontal extent of the aurora along the line of sight is unknown (Schneider et al., 2021), making it difficult to convert limb observations to vertical column brightness and to determine the real altitude of the emission peak.

Recent observations with the SWEA instrument on board MAVEN indicate that, in most cases, the electron precipitation is soft. The mean energy has not been analyzed but the peak of the auroral electron flux is statistically on the order of 100 eV (Xu et al., 2022b). More energetic precipitation has been observed during inverted V acceleration (Xu et al., 2020), but such events appear to be rare. These results are in line with our Monte Carlo simulations with the MCD atmosphere indicating that the observed mean Cameron/UV doublet intensity ratio requires relatively soft (E < 100 eV) electron precipitation. Higher values of the mean electron energy have been reported by Gérard et al. (2015), but they correspond to the bright events observed with SPICAM, as detection of weaker aurorae was limited by the sensitivity threshold of the instrument. We note that the case of the diffuse aurora where high-energy electrons and protons produce auroral ultraviolet emissions peaking below 100 km (Nakamura et al., 2022) is not considered here. In this case, the $a^3\Pi$ state is deactivated by collisions with CO_2 (Gérard et al., 2017), unlike in the discrete aurora considered in this study.

Finally, the reduction of the Cameron emission cross section for electron impact on CO_2 should also affect the dayglow, as was briefly discussed in Lee et al. (2022). They showed that the mean energy of the photoelectrons in the dayglow is 21.5 eV near 130 km, in agreement with model calculations of the electron energy degradation in the sunlit Martian atmosphere. At this energy, the Lee et al. cross section is a factor 3 to 4 smaller than the Avakyan-Shirai value. They argued that the effect of the change in the predicted Cameron band dayglow intensity is mitigated by the presence of additional source processes such as photodissociation of CO_2 into the CO a $^3\Pi$ state. Jain and Bhardwaj (2012) and Gérard et al. (2017) showed that photodissociation of CO_2 is indeed a significant source of CO a $^3\Pi$ state at the altitude of the dayglow emission peak. Further work is needed to assess the effect of the new cross section values on the Mars and Venus dayglow.

Declaration of Competing Interest

Authors declare that they have no competing interest.

Data availability

Atmospheric temperature and densities from the Mars Climate Database are available from the 5.3 version of the MCD data at http://www-mars.lmd.jussieu.fr. The GEM-Mars values and model simulations of auroral emission rates are available from the authors on request.

Acknowledgements

B. Hubert is a research associate of the Belgian Fund for Scientific Research (FNRS). L. Soret and J.-C. Gérard acknowledge support from the Belgian Federal Science Policy Office, with financial and contractual coordination by the ESA PRODEX Office (PEA Grant No. 4000121493).

Appendix A. Supplementary data

Supplementary data to this article can be found online at https://doi.org/10.1016/j.icarus.2023.115602.

References

Ajello, J.M., 1971a. Emission cross sections of CO by electron impact in the interval 1260–5000 Å. I. J. Chem. Phys. 55 (7), 3158–3168.
Ajello, J.M., 1971b. Emission cross sections of CO_2 by electron impact in the interval 1260–4500 Å. II. J. Chem. Phys. 55 (7), 3169–3177.

Avakyan, S.V., Ii'In, R.N., Lavrov, V.M., Ogurtsov, G.N., 1999. Collision Processes and Excitation of UV Emission from Planetary Atmospheric Gases: A Handbook of Cross Sections. CRC Press.

Barth, C.A., Hord, C.W., Pearce, J.B., Kelly, K.K., Anderson, G.P., Stewart, A.I., 1971. Mariner 6 and 7 ultraviolet spectrometer experiment: upper atmosphere data. J. Geophys. Res. 76 (10), 2213–2227.

Barth, C.A., Stewart, A.I., Hord, C.W., Lane, A.L., 1972. Mariner 9 ultraviolet spectrometer experiment: Mars airglow spectroscopy and variations in Lyman alpha. Icarus 17 (2), 457–468.

Bertaux, J.L., Leblanc, F., Witasse, O., Quemerais, E., Lilensten, J., Stern, S.A., Korablev, O., 2005. Discovery of an aurora on Mars. Nature 435 (7043), 790–794.

Bhardwaj, A., Jain, S.K., 2009. Monte Carlo model of electron energy degradation in a CO_2 atmosphere. J. Geophys. Res. Space Physics 114 (A11).

Bisikalo, D.V., Shematovich, V.I., Gérard, J.-C., et al., 2017. Influence of the crustal magnetic field on the Mars aurora electron flux and UV brightness. Icarus 282, 127–135.

Bougher, S.W., Pawlowski, D., Bell, J.M., Nelli, S., McDunn, T., Murphy, J.R., Ridley, A., 2015. Mars global ionosphere-thermosphere model: solar cycle, seasonal, and diurnal variations of the Mars upper atmosphere. J. Geophys. Res.: Planet. 120 (2), 311–342.

Conway, R.R., 1981. Spectroscopy of the Cameron bands in the Mars airglow. J. Geophys. Res. Space Physics 86 (A6), 4767–4775.

Cox, C., Gérard, J.C., Hubert, B., Bertaux, J.L., Bougher, S.W., 2010. Mars ultraviolet dayglow variability: SPICAM observations and comparison with airglow model. J. Geophys. Res.: Planet. 115 (E4).

Daerden, F., Neary, L., Viscardy, S., García Muñoz, A., Clancy, R.T., Smith, M.D., et al., 2019. Mars atmospheric chemistry simulations with the GEM-Mars general circulation model. Icarus 326, 197–224.

Deighan, J., Jain, S.K., Chaffin, M.S., Fang, X., Halekas, J.S., Clarke, J.T., Jakosky, B.M., 2018. Discovery of a proton aurora at Mars. Nat. Astronom. 2 (10), 802–807.

Erdman, P.W., Zipf, E.C., 1983. Electron-impact excitation of the Cameron system ($a^3\Pi \rightarrow X^1\Sigma$) of CO. Planet. Space Sci. 31 (3), 317–321.

Evans, J.S., Correira, J., Deighan, J., Jain, S., Al Matroushi, H., Al Mazmi, H., Thiemann, E., 2022. Retrieval of CO relative column abundance in the Martian thermosphere from FUV disk observations by EMM EMUS. Geophys. Res. Lett. 49 (18), e2022GL099615.

Forget, F., Hourdin, F., Fournier, R., Hourdin, C., Talagrand, O., Collins, M., Huot, J.P., 1999. Improved general circulation models of the Martian atmosphere from the surface to above 80 km. J. Geophys. Res.: Planet. 104 (E10), 24155–24175.

Fournier, J.A., Shuman, N.S., Melko, J.J., Ard, S.G., Viggiano, A.A., 2013. A novel technique for measurement of thermal rate constants and temperature dependences of dissociative recombination: CO_2^+, CF_3^+, N_2O^+, $C_7H_8^+$, $C_7H_7^+$, $C_6H_6^+$, $C_6H_5^+$, $C_5H_6^+$, $C_4H_4^+$, and $C_3H_3^+$. J. Chem. Phys. 138 (15), 154201.

Fox, J.L., Dalgarno, A., 1979. Ionization, luminosity, and heating of the upper atmosphere of Mars. J. Geophys. Res. 84 (A12), 7315–7333.

Fox, J.L., Dalgarno, A., 1981. Ionization, luminosity, and heating of the upper atmosphere of Venus. J. Geophys. Res. Space Physics 86 (A2), 629–639.

Fox, J.L., Johnson, A.S., Ard, S.G., Shuman, N.S., Viggiano, A.A., 2017. Photochemical determination of O densities in the Martian thermosphere: effect of a revised rate coefficient. Geophys. Res. Lett. 44, 8099–8106. https://doi.org/10.1002/2017GL074562.

Freund, R.S., 1971. Dissociation of CO_2 by electron impact with the formation of metastable CO ($a\ ^3\Pi$) and O (^5S). J. Chem. Phys. 55 (7), 3569–3577.

Furlong, J.M., Newell, W.R., 1996. Total cross section measurement for the metastable a $^3\Pi$ state in CO. J. Phys. B Atomic Mol. Phys. 29, 331–338.

Gérard, J.C., Hubert, B., Shematovich, V.I., Bisikalo, D.V., Gladstone, G.R., 2008. The Venus ultraviolet oxygen dayglow and aurora: model comparison with observations. Planet. Space Sci. 56, 542–552.

Gérard, J.C., Soret, L., Libert, L., Lundin, R., Stiepen, A., Radioti, A., Bertaux, J.L., 2015. Concurrent observations of ultraviolet aurora and energetic electron precipitation with Mars express. J. Geophys. Res. Space Physics 120 (8), 6749–6765.

Gérard, J.C., Soret, L., Shematovich, V.I., Bisikalo, D.V., Bougher, S.W., 2017. The Mars diffuse aurora: a model of ultraviolet and visible emissions. Icarus 288, 284–294. https://doi.org/10.1016/j.icarus.2017.01.037.

González-Galindo, F., Forget, F., López-Valverde, M.A., Angelats i Coll, M., Millour, E., 2009. A ground-to-exosphere Martian general circulation model: 1. Seasonal, diurnal, and solar cycle variation of thermospheric temperatures. J. Geophys. Res.: Planet. 114 (E4).

González-Galindo, F., Chaufray, J.-Y., López-Valverde, M.A., Gilli, G., Forget, F., Leblanc, F., Modolo, R., Hess, S., Yagi, M., 2013. Three-dimensional Martian ionosphere model: I. the photochemical ionosphere below 180 km. J. Geophys. Res. Planets 118, 2105–2123. https://doi.org/10.1002/jgre.20150.

González-Galindo, F., Chaufray, J.Y., Forget, F., García-Comas, M., Montmessin, F., Jain, S.K., Stiepen, A., 2018. UV dayglow variability on Mars: simulation with a global climate model and comparison with SPICAM/MEx data. J. Geophys. Res.: Planet. 123 (7), 1934–1952.

Gronoff, G., Simon Wedlund, C., Mertens, C.J., Barthélemy, M., Lillis, R.J., Witasse, O., 2012. Computing uncertainties in ionosphere-airglow models: II. The Martian airglow. J. Geophys. Res. Space Physics 117 (A5).

Haider, S.A., Mahajan, K.K., Kallio, E., 2011. Mars ionosphere: A review of experimental results and modeling studies. Rev. Geophys. 49 (4).

Itikawa, Y., 2002. Cross sections for electron collisions with carbon dioxide. J. Phys. Chem. Ref. Data 31 (3), 749–767.

Jain, S.K., Bhardwaj, A., 2012. Impact of solar EUV flux on CO Cameron band and CO_2^+ UV doublet emissions in the dayglow of Mars. Planet. Space Sci. 63, 110–122.

Jain, S.K., Stewart, A.I.F., Schneider, N.M., Deighan, J., Stiepen, A., Evans, J.S., Jakosky, B.M., 2015. The structure and variability of Mars upper atmosphere as seen in MAVEN/IUVS dayglow observations. Geophys. Res. Lett. 42 (21), 9023–9030.

Leblanc, F., Chaufray, J.Y., Lilensten, J., Witasse, O., Bertaux, J.L., 2006. Martian dayglow as seen by the SPICAM UV spectrograph on Mars express. J. Geophys. Res.: Planet. 111 (E9).

Leblanc, F., Witasse, O., Lilensten, J., Frahm, R.A., Safaenili, A., Brain, D.A., Lundin, R., 2008. Observations of aurorae by SPICAM ultraviolet spectrograph on board Mars express: simultaneous ASPERA-3 and MARSIS measurements. J. Geophys. Res. Space Physics 113 (A8).

Lee, R.A., Ajello, J.M., Malone, C.P., Evans, J.S., Veibell, V., Holsclaw, G.M., Schneider, N.M., 2021. Laboratory study of the Cameron bands, the first negative bands, and fourth positive bands in the middle ultraviolet 180–280 nm by electron impact upon CO. J. Geophys. Res.: Planet. 126 (1) e2020JE006602.

Lee, R.A., Joseph, M. Ajello, Malone, Charles P., Evans, J. Scott, Veibell, Victoir, Holsclaw, Gregory M., McClintock, William E., Hoskins, Alan C., Jain, Sonal K., Gérard, J.C., Aryal, S.A., Schneider, N.M., 2022. Laboratory study of the Cameron bands and UV doublet in the middle ultraviolet 180–300 nm by electron impact upon CO_2 with application to Mars. Astrophys. J. 938 https://doi.org/10.3847/1538-4357/ac88c8.

Lillis, R.J., Deighan, J., Brain, D., Fillingim, M., Jain, S., Chaffin, M., et al., 2022. First synoptic images of FUV discrete aurora and discovery of sinuous aurora at Mars by EMM EMUS. Geophys. Res. Lett. 49 https://doi.org/10.1029/2022GL099820 e2022GL099820.

Mahaffy, P.R., Benna, M., Elrod, M., Yelle, R.V., Bougher, S.W., Stone, S.W., Jakosky, B. M., 2015. Structure and composition of the neutral upper atmosphere of Mars from the MAVEN NGIMS investigation. Geophys. Res. Lett. 42, 8951–8957. https://doi.org/10.1002/2015GL065329.

McClintock, W.E., Schneider, N.M., Holsclaw, G.M., Clarke, J.T., Hoskins, A.C., Stewart, I., Deighan, J., 2015. The imaging ultraviolet spectrograph (IUVS) for the MAVEN mission. Space Sci. Rev. 195, 75–124.

Millour, E., Francois, F., Aymeric, S., Margaux, V., Vladimir, Z., Luca, M., et al., 2019. The Mars climate database (MCD version 5.3). Geophysical Research Abstracts, 21, EGU General Assembly 2019.

Nakamura, Y., Terada, N., Leblanc, F., Rahmati, A., Nakagawa, H., Sakai, S., Murase, K., 2022. Modeling of diffuse auroral emission at Mars: Contribution of MeV protons. J. Geophys. Res. Space Phys. 127 (1) e2021JA029914.

Neary, L., Daerden, F., 2018. The GEM-Mars general circulation model for Mars: description and evaluation. Icarus 300, 458–476.

Nier, A.O., McElroy, M.B., 1977. Composition and structure of Mars' upper atmosphere: results from the neutral mass spectrometers on Viking 1 and 2. J. Geophys. Res. 82, 4341–4349.

Ritter, B., Gérard, J.C., Hubert, B., Rodriguez, L., Montmessin, F., 2018. Observations of the proton aurora on Mars with SPICAM on board Mars express. Geophys. Res. Lett. 45 (2), 612–619.

Rosati, R.E., Johnsen, R., Golde, M.F., 2003. Absolute yields of CO ($a'\ ^3\Sigma+$, $d\ ^3\Delta$ i, $e\ ^3\Sigma-$) + O from the dissociative recombination of CO_2^+ ions with electrons. J. Chem. Phys. 119 (22), 11630–11635.

Schneider, N.M., Deighan, J.I., Jain, S.K., Stiepen, A., Stewart, A.I.F., Larson, D., Jakosky, B.M., 2015. Discovery of diffuse aurora on Mars. Science 350 (6261), aad0313.

Schneider, N.M., Milby, Z., Jain, S.K., Gérard, J.C., Soret, L., Brain, D.A., Jakosky, B.M., 2021. Discrete Aurora on Mars: insights into their distribution and activity from MAVEN/IUVS observations. J. Geophys. Res. Space Physics 126 (10) e2021JA029428.

Shematovich, V.I., Bisikalo, D.V., Gérard, J.C., 1994. A kinetic model of the formation of the hot oxygen geocorona: 1. Quiet geomagnetic conditions. J. Geophys. Res. Space Physics 99 (A12), 23217–23228.

Shematovich, V.I., Bisikalo, D.V., Gérard, J.-C., Cox, C., Bougher, S.W., Leblanc, F., 2008. Monte Carlo model of electron transport for the calculation of Mars dayglow emissions. J. Geophys. Res. 113, E02011. https://doi.org/10.1029/2007JE002938.

Shirai, T., Tabata, T., Tawara, H., 2001. Analytic cross sections for electron collisions with CO, CO_2, and H_2O relevant to edge plasma impurities. At. Data Nucl. Data Tables 79, 143–184.

Skrzypkowski, M.P., Gougousi, T., Johnsen, R., Golde, M.F., 1998. Measurement of the absolute yield of CO ($a\ ^3\Pi$)+ O products in the dissociative recombination of CO_2^+ ions with electrons. J. Chem. Phys. 108 (20), 8400–8407.

Soret, L., Gérard, J.C., Libert, L., Shematovich, V.I., Bisikalo, D.V., Stiepen, A., Bertaux, J. L., 2016. SPICAM observations and modeling of Mars aurorae. Icarus 264, 398–406.

Soret, L., Gérard, J.C., Schneider, N., Jain, S., Milby, Z., Ritter, B., Weber, T., 2021. Discrete aurora on Mars: spectral properties, vertical profiles, and electron energies. J. Geophys. Res. Space Physics 126 (10) e2021JA029495.

Stewart, A.I., Barth, C.A., Hord, C.W., Lane, A.L., 1972. Mariner 9 ultraviolet spectrometer experiment: structure of Mars' upper atmosphere. Icarus 17, 469–474.

Tsurubuchi, S., Iwai, T., 1974. Simultaneous ionization and excitation of CO_2 by electron-impact. J. Phys. Soc. Jpn. 37 (4), 1077–1081.

Viggiano, A.A., Ehlerding, A., Hellberg, F., Thomas, R.D., Zhaunerchyk, V., Geppert, W. D., Österdahl, F., 2005. Rate constants and branching ratios for the dissociative recombination of CO_2^+. J. Chem. Phys. 122 (22), 226101.

Wu, X.-S., Cui, J., Yelle, R.V., Cao, Y.-T., He, Z.-G., He, F., et al., 2020. Photoelectrons as a tracer of planetary atmospheric composition: application to CO on Mars. J. Geophys. Res.: Planet. 125 e2020JE006441.

Xu, S., Mitchell, D.L., McFadden, J.P., Fillingim, M.O., Andersson, L., Brain, D.A., Espley, J., 2020. Inverted-V electron acceleration events concurring with localized auroral observations at Mars by MAVEN. Geophys. Res. Lett. 47 (9) e2020GL087414.

Xu, S., Mitchell, D.L., McFadden, J.P., Schneider, N.M., Milby, Z., Jain, S., Johnston, B., 2022a. Empirically determined Auroral electron events at Mars—MAVEN observations. Geophys. Res. Lett. 49 (6) e2022GL097757.

Xu, S., Mitchell, D.L., McFadden, J.P., Fowler, C.M., Hanley, K., Weber, T., Curry, S.M., 2022b. Nightside auroral electrons at Mars upstream drivers and ionospheric impact. J. Geophys. Res. Space Physics 49 (6) e2022JA030801.

Yoshida, N., Terada, N., Nakagawa, H., Brain, D.A., Sakai, S., Nakamura, Y., et al., 2021. Seasonal and dust-related variations in the dayside thermospheric and ionospheric compositions of Mars observed by MAVEN/NGIMS. J. Geophys. Res.: Planet. 126 https://doi.org/10.1029/2021JE006926 e2021JE006926.

Yoshida, N., Nakagawa, H., Aoki, S., Erwin, J., Vandaele, A.C., Daerden, F., Patel, M., 2022. Variations in vertical CO/CO_2 profiles in the Martian mesosphere and lower thermosphere measured by the ExoMars TGO/NOMAD: implications of variations in eddy diffusion coefficient. Geophys. Res. Lett. 126, e2022GL098485.